Journal of Catalysis 368 (2018) 134–144

Contents lists available at ScienceDirect

Journal of Catalysis

journal homepage: www.elsevier.com/locate/jcat

SiO_2@V_2O_5@Al_2O_3 core–shell catalysts with high activity and stability for methane oxidation to formaldehyde

Euiseob Yang [a], Jun Gyeong Lee [a], Dong Hyeon Kim [a,b], Yoon Seok Jung [b], Ja Hun Kwak [a], Eun Duck Park [c,*], Kwangjin An [a,*]

[a] School of Energy and Chemical Engineering, Ulsan National Institute of Science and Technology(UNIST), Ulsan 44919, Republic of Korea
[b] Department of Energy Engineering, Hanyang University, Seoul 04763, Republic of Korea
[c] Department of Chemical Engineering and Department of Energy Systems Research, Ajou University, Suwon 16499, Republic of Korea

ARTICLE INFO

Article history:
Received 21 May 2018
Revised 16 August 2018
Accepted 24 September 2018

Keywords:
Vanadium
V_2O_5
Core@shell
Methane oxidation
Formaldehyde
Stable catalyst

ABSTRACT

The stable tetrahedral geometry and high C—H bond dissociation energy of methane complicate its direct catalytic conversion; for example, the selective oxidation of methane to formaldehyde, which avoids the production of carbon dioxide by full oxidation and is therefore important for the versatile utilization of natural gas, is still viewed as challenging. Here, we utilize hydrothermal synthesis followed by atomic layer deposition (ALD) to prepare an efficient and thermally stable catalyst based on novel SiO_2@V_2O_5@Al_2O_3 core@shell nanostructures, showing that the thickness of Al_2O_3 shells over SiO_2@V_2O_5 cores can be tuned by controlling the number of ALD cycles. Catalytic methane oxidation experiments performed in a flow reactor at 600 °C demonstrate that SiO_2@V_2O_5@Al_2O_3 nanostructures obtained after 50 ALD cycles exhibit the best catalytic activity (methane conversion = 22.2%; formaldehyde selectivity = 57.8%) and outperform all previously reported vanadium-based catalysts at 600 °C. The prepared catalysts are subjected to in-depth characterization, which reveals that their Al_2O_3 shell provides new surfaces for the generation of highly disperse T_d monomeric species with a V—O—Al bond by promoting interactions between Al_2O_3 and V_2O_5 nanoparticles during ALD. Moreover, the surface Al_2O_3 shell is found not only to protect V_2O_5 nanoparticles against sintering at 600 °C, but also to anchor the produced T_d monomeric vanadium species responsible for the high catalytic performance.

1. Introduction

Methane, the main component of natural gas, is mainly used for heating and electricity generation [1–3]. Recent progress in shale gas collection technology based on hydraulic fracturing presents a further stimulus for converting abundant methane to more valuable chemical feedstocks and thus reducing dependence on petroleum resources [1]. Nevertheless, the four strong C—H bonds of methane (bond energy = 413 kJ mol^{-1}) present a serious obstacle to its chemical conversion. At elevated temperatures, methane can be catalytically converted to syngas, which can be used as a feedstock for the catalytic production of added-value hydrocarbons or alcohols. Although a number of indirect processes for the oxidative conversion of methane to formaldehyde (HCHO), methanol (CH_3OH), and ethylene (C_2H_4) have been developed and applied industrially [4–8], direct conversion of methane by partial oxidation is still challenging in view of the abovementioned high C—H bond energy and the need to avoid the production of carbon dioxide as a greenhouse gas [9]. Previous studies on methane oxidation to HCHO demonstrated that temperatures above 600 °C are required to break the strong C—H bonds and identified supported V_2O_5 and MoO_3 as the best partial oxidation catalysts for producing HCHO or CH_3OH [10–12]. However, HCHO easily undergoes further oxidation to CO and H_2O, which requires the development of efficient partial oxidation catalysts, for example, by modifying the above catalysts while preserving their high-temperature active sites. Notably, the use of noble metals such as Pt or Pd for C—H bond activation results in the complete oxidation of methane to CO, CO_2, and H_2O [13–16]. For these reasons, the partial oxidation of methane to HCHO is still regarded as a challenging reaction, and the best methane-to-HCHO conversion achieved so far at 600 °C is less than 10%. Parmaliana et al. reported that conversions of 1–3% obtained at 600 °C for V_2O_5/SiO_2 catalysts prepared by impregnation further increased to 25% at 700 °C, although the HCHO selectivity was less than 30% [10]. Nguyen et al. used mesoporous silicas to prepare several impregnated V_2O_5/SiO_2 catalysts [11],

* Corresponding authors.
E-mail addresses: edpark@ajou.ac.kr (E.D. Park), kjan@unist.ac.kr (K. An).

https://doi.org/10.1016/j.jcat.2018.09.027
0021-9517/

since silica was identified as the best support for V_2O_5-based catalysts for methane partial oxidation [10–13,17–20], achieving methane-to-HCHO conversion and selectivity of 6.3 and 58%, respectively, at 600 °C [11].

The thermal stability of catalytically active surface species can be increased by protection/encapsulation with robust oxide(s). In well-designed core@shell-type catalysts, highly disperse active species in the core can be protected against deactivation caused by sintering or coking during high-temperature reactions [21–31]. Atomic layer deposition (ALD) is considered an attractive thin film growth technique for homogeneous encapsulation of active species, allowing the surfaces of core species to be uniformly coated with layers of controlled thickness at an atomic scale [32–35]. In view of the fact that overly thick ALD coatings reduce the activity of core catalysts, the abovementioned control of coating layer thickness is critical for the maximization of catalyst activity/stability and for the preservation of active species under severe reaction conditions.

Here, we designed highly disperse V_2O_5 nanocatalysts supported on SiO_2 spheres for the direct oxidation of methane to HCHO, utilizing a hydrothermal reaction to attach V_2O_5 nanoparticles uniformly to the surfaces of SiO_2 spheres. The original structure of V_2O_5 nanoparticles collapsed at temperatures above 300 °C, which was mitigated by further coating SiO_2@V_2O_5 core@shell structures via the alumina ALD with trimethylaluminum (TMA) as an alumina source [36]. Multicycle ALD coating afforded controlled-layer-thickness SiO_2@V_2O_5@Al_2O_3 core@shell nanostructures, which were used for the catalytic oxidation of methane to HCHO in a plug-flow fixed-bed reactor at 600 °C. Whereas negligible conversion was observed for SiO_2@V_2O_5 catalysts without alumina shells because of V_2O_5 nanoparticle sintering, SiO_2@V_2O_5@Al_2O_3 core@shell nanostructures exhibited increased thermal stability at 600 °C which depended on the thickness of their alumina coatings. Transmission electron microscopy (TEM), scanning electron microscopy (SEM), energy-dispersive X-ray spectroscopy (EDS), in situ X-ray diffraction (XRD), Raman spectroscopy, H_2 temperature-programmed reduction (H_2 TPR), and diffuse reflectance UV–vis spectroscopy analyses were used to determine the mechanism of core vanadium species preservation at high temperature and the type of core@shell structures achieving maximal methane-to-HCHO conversion without undergoing deactivation. Compared with conventional mesoporous silica (m-SiO_2)-supported V_2O_5 catalysts prepared by impregnation, SiO_2@V_2O_5@Al_2O_3 core@shell nanostructures achieved exceptionally high methane conversion and featured increased stability, which was ascribed to the presence of alumina shells over V_2O_5 nanoparticles.

2. Experimental

2.1. Preparation of SiO_2@V_2O_5 nanostructures

Silica spheres were synthesized by the Stöber method [37]. Briefly, NH_4OH (7.5 mL) and H_2O (24 mL) were dispersed in ethanol (294 mL) under vigorous stirring at room temperature. Tetraethyl orthosilicate (TEOS; Aldrich, 98%, 15 mL) was added dropwise to the obtained solution, and the reaction mixture was stirred for 24 h further. The resulting opaque solution was filtered, and the filter cake was washed with ethanol and dried at 70 °C to obtain silica spheres. To synthesize SiO_2@V_2O_5 core@shell nanostructures, as-prepared silica spheres (0.3 g) were mixed with vanadyl acetylacetonate ($VO(acac)_2$; Sigma-Aldrich, 97%, 0.83 g) in dimethylformamide (40 mL) under 3 h sonication [38]. The obtained dispersion was placed in a 50 mL Teflon-lined autoclave reactor and heated at 220 °C for 24 h. The dark precipitate was separated by centrifugation, washed with ethanol, dried at 70 °C, and calcined at 400 °C for 3 h to obtain SiO_2@V_2O_5 core@shell nanostructures.

2.2. Preparation of SiO_2@V_2O_5@Al_2O_3-(x) (x = 10, 30, 40, 50, 70, and 100) core@shell nanostructures

Al_2O_3 shells were grown on SiO_2@V_2O_5 core@shell structures in a rotary ALD reactor using a TMA (Sigma-Aldrich, 97%; alumina precursor)–Ar–H_2O–Ar sequence [36]. An overview of the ALD equipment is provided in Scheme S1 in the Supplementary Material. First, SiO_2@V_2O_5 powders were loaded into a porous stainless steel cylinder that was rotated at 140 rpm inside the reaction chamber. For a single cycle of the ALD sequence, TMA introduced at a pressure of 2 Torr was deposited onto V_2O_5 surfaces at 180 °C, and the chamber was subsequently evacuated to remove CH_4 generated as a byproduct and unreacted TMA. The chamber was filled with Ar to a pressure of 20 Torr and evacuated after several minutes. Then H_2O (2 Torr) was introduced to replace the methyl groups of the attached TMA with OH groups, and the chamber was evacuated to remove the produced CH_4 and excess H_2O and purged with Ar (20 Torr). For the second cycle, the above steps were repeated. The number of cycles was denoted as (x) and was found to be proportional to the thickness of Al_2O_3 shells. SiO_2@V_2O_5@Al_2O_3-(x) core@shell nanostructures with controlled Al_2O_3 shell thickness were prepared using different numbers of ALD cycles (x = 10, 30, 40, 50, 70, and 100).

2.3. Preparation of mesoporous silica-supported V_2O_5 (V_2O_5/m-SiO_2) catalysts

Conventional V_2O_5/m-SiO_2 catalysts were prepared by incipient wetness impregnation. Mesoporous silica with a mesocellular structure (MCF-17) prepared by a previously described method was used as a support [39]. Briefly, 1,3,5-trimethylbenzene (Sigma-Aldrich, 98%; 4 g) was dissolved in 75 mL of an aqueous solution containing 4 g of Pluronic P123 triblock copolymer (Aldrich, average $M_w \approx 5800$ Da) and 10 mL of concentrated HCl. The reaction mixture was stirred for 2 h at 40 °C and then treated with TEOS (9.2 mL) and maintained for 5 min. The resulting solution was kept at 40 °C for 20 h without stirring, treated with NH_4F (Sigma-Aldrich, 98%; 46 mg), and further aged in a closed bottle at 100 °C for another 24 h. The obtained white precipitate was filtered, washed with water and ethanol, and calcined in air at 600 °C for 6 h to obtain MCF-17. V_2O_5/m-SiO_2 catalysts were prepared by exposing MCF-17 (1 g) overnight to a solution of ammonium vanadium oxide (NH_4VO_3, Alfa Aesar, 99%) in the presence of oxalic acid dihydrate ($C_2H_2O_4{\cdot}2H_2O$, Acros Organics, 99%). Centrifugation followed by drying afforded solid V_2O_5/m-SiO_2 catalysts with vanadium precursor loadings of 1, 3, and 5 wt% after calcination at 350 °C for 4 h. Conventional V_2O_5/Al_2O_3 catalysts were also prepared by the same impregnation method in the presence of commercial Al_2O_3 (Puralox SBa 200, Sasol) for comparison. In detail, 1 g of Al_2O_3 was mixed with oxalic acid dihydrate in an ethanol solution of NH_4VO_3. After drying at 60 °C and calcination at 350 °C 4 h, 3 and 5 wt% of V_2O_5/Al_2O_3 catalysts were obtained.

2.4. Characterization

Powder and in situ XRD patterns were acquired in a 2θ range of 20–80° (Cu K_α radiation, λ = 1.5418 Å) using PANalytical X'Pert Pro and Rigaku SmartLab X-ray diffractometers, respectively. Prior to measurements, samples were loaded onto a holder and preheated at 150 °C for 30 min under Ar. In situ spectra were recorded for catalysts exposed to a heated gas mixture of 4% CH_4, 4% O_2, and balance Ar in steps of 50 °C from 100 to 800 °C using a specially constructed cell. Brunauer–Emmett–Teller (BET) surface areas

were determined from N_2 adsorption/desorption isotherms recorded on a microtrac BELsorp-Max analyzer (Table S1 in the Supplementary Material). Pore size distributions were determined by the Barrett–Joyner–Halenda method. SEM imaging was performed using a Hitachi S-4800 microscope, and TEM imaging was performed using a JEOL JEM-2100F instrument operated at 200 kV. An EDS analyzer was used for elemental analysis (Oxford Instruments, X-Max 80 T). TPR was carried out on the abovementioned Micromeritics AutoChem II 2920 instrument. Typically, a catalyst sample (100 mg) was loaded into a U-shaped quartz tube and outgassed under He flow at 150 °C for 30 min. Subsequently, the temperature was increased to 800 °C at a rate of 10 °C min^{-1} in a flow of 10% H_2 in He (50 mL min^{-1}). The amount of H_2 consumed was determined by gas chromatography using a Delsi Nermag thermal conductivity detector. Diffuse reflectance UV–vis spectra were recorded with a scan step of 1 nm on an Agilent Cary 5000 UV–vis–NIR spectrophotometer operated in the region 200–2200 nm. A halon white (PTFE) reflectance standard was used as a reference background. Raman spectra were collected utilizing a WITec alpha300 R spectrometer equipped with a 532 nm diode laser. The laser power was set to 0.1 mW. To obtain sufficient signal-to-noise ratios, spectra were obtained using CCD with 10-s exposure and 10-fold accumulation.

2.5. Methane oxidation

Catalytic methane oxidation was conducted in a laboratory-scale flow reactor at atmospheric pressure and a constant temperature of 600 °C. As-synthesized vanadium-based catalysts were pelletized and sieved to a particle size of 150–250 μm. A 100 mg catalyst sample was loaded into a quartz tube (inner diameter 1 cm) together with 1 g of purified sand. CH_4 (99.95%) and O_2 (99.995%) in a 1:1 v/v ratio were fed from the top to the bottom of the catalyst bed at a rate of 40 sccm using mass flow controllers, and the gas hourly space velocity (GHSV) was maintained at 24,000 mL g_{cat}^{-1} h^{-1}. The reactor was heated to 600 °C in a furnace and equipped with an inserted thermocouple to monitor temperature. Products were monitored using an online gas chromatograph (YL6500) equipped with Porapak-N and molecular sieve columns connected to both thermal conductivity and flame ionization detectors with a methanizer (Ar was flowed in as a reference). No methane conversion was detected when empty quartz or bare SiO_2 spheres without V_2O_5 were tested. HCHO, CO, CO_2, and H_2 were identified as the main reaction products. Before the converted gases entered the gas chromatograph, HCHO was trapped in 10.5 g of Na_2SO_3 and 1.63 g of H_2SO_4 cooled in an ice bath, and the amount of trapped HCHO was determined by titrating the produced NaOH with H_2SO_4 [11,40,41]. Methane conversion was calculated as the ratio of consumed and original methane amounts using gas chromatography data for points in stabilized areas with maximum activity values. Selectivity was calculated as the ratio of product amount and total converted methane amount. The conversion of $SiO_2@V_2O_5@Al_2O_3$-(x) core@shell nanostructures (x = 40, 50, and 70) was determined by the average value of methane conversions, in which each reaction was conducted more than three times for reproducibility. We calculated turnover frequency (TOF_{HCHO}) by the number of CH_4 molecules reacted to HCHO on each available vanadium site per time. By assuming that an isolated vanadium species on the outermost surface of the V_2O_5 nanoparticles was contacted with the alumina shell, the total surface area of the core@shell catalyst was determined by the size and mass of the structure. SiO_2 spheres with an average diameter of 150 nm were wrapped in V_2O_5 with a thickness of ca. 35 nm. The mass of a single nanostructure was obtained by multiplying the volume and density that were calculated from the BET measurement. The number of core@shell nanostructures was estimated by the mass of a single nanoparticle; thus the total surface area and the isolated surface vanadium sites (7.3×10^{18}) were finally determined for the TOFs.

3. Results and discussion

3.1. Preparation of $SiO_2@V_2O_5@Al_2O_3$ core@shell catalysts

As mentioned above, $SiO_2@V_2O_5@Al_2O_3$ core@shell nanostructures were prepared by hydrothermal synthesis followed by ALD (Fig. 1a), and SiO_2 spheres with an average size of 150 nm were synthesized using the well-known Stöber method [37] (Fig. 1b). Discrete V_2O_5 nanoparticles with an average size of 35 nm were deposited on the surfaces of SiO_2 spheres by a hydrothermal reac-

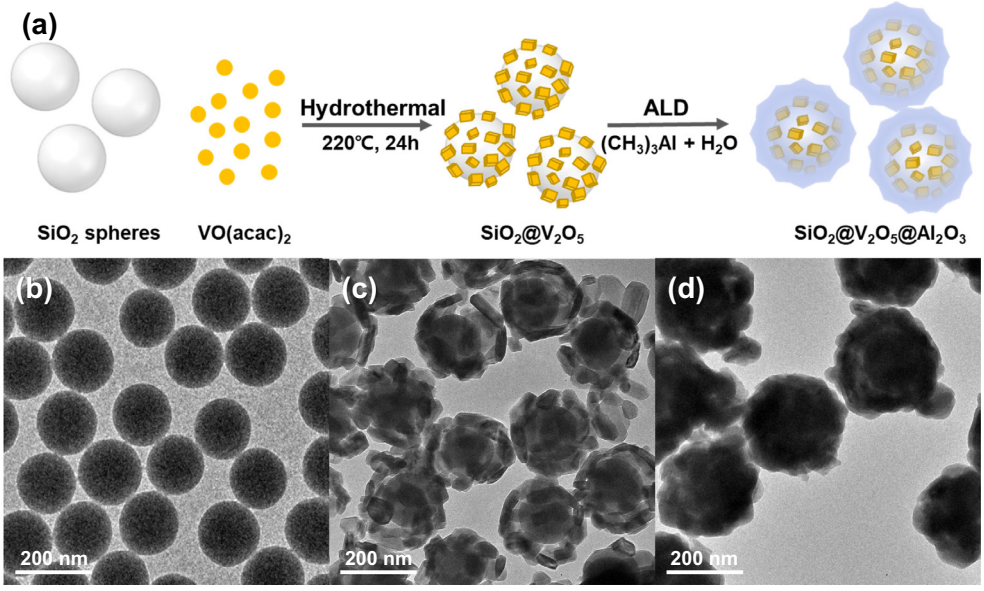

Fig. 1. (a) Schematic preparation of $SiO_2@V_2O_5@Al_2O_3$ core@shell nanostructures. TEM images of (b) SiO_2 spheres, (c) $SiO_2@V_2O_5$, and (d) $SiO_2@V_2O_5@Al_2O_3$-(50) core@shell nanostructures.

tion in the presence of $VO(acac)_2$ (Fig. 1c). During the reaction, small vanadium clusters were first formed by nucleation, and then the vanadium species were mostly attached to SiO_2 spheres, because of the hydrophilic nature of the SiO_2 surface. By subsequent ALD with various numbers of repeating cycles, thin Al_2O_3 layers were deposited over $SiO_2@V_2O_5$ core@shells with a controlled thickness. Fig. 1d shows a TEM image of representative $SiO_2@V_2O_5@Al_2O_3$-(50) core@shell nanostructures, unambiguously demonstrating the presence of Al_2O_3 layers coating the core structures.

The surface morphology of $SiO_2@V_2O_5@Al_2O_3$-(50) core@shell nanostructures was investigated by SEM, scanning TEM (STEM), and EDS. Fig. 2a clearly demonstrates that outer Al_2O_3 layers were homogeneously deposited on the entire surface of $SiO_2@V_2O_5$ nanostructures. STEM imaging and the corresponding elemental mappings with EDS line scanning (Fig. 2b) showed that O and V (derived from V_2O_5) were uniformly dispersed in the shell, while Si (derived from silica spheres) was mainly located in the core. Moreover, the distribution of alumina over the whole core@shell nanostructures demonstrated that they were coated by thin Al_2O_3 shell layers. $SiO_2@V_2O_5@Al_2O_3$-(10, 30, 50, and 100) core@shell nanostructures were also characterized by high-resolution TEM (Fig. S1), which revealed that 100 ALD cycles were sufficient to obtain full coverage by 20-nm-thick Al_2O_3 layers, while 10 cycles did not suffice for an effective coating.

The shell thickness of $SiO_2@V_2O_5@Al_2O_3$ core@shell nanostructures increased with the number of ALD cycles (Fig. 3a). The introduced TMA precursor was adsorbed onto V_2O_5 surfaces to create Al—O bonds, and $Al(OH)_4$ units (together with methane) were finally produced upon the addition of water vapor. Subsequent

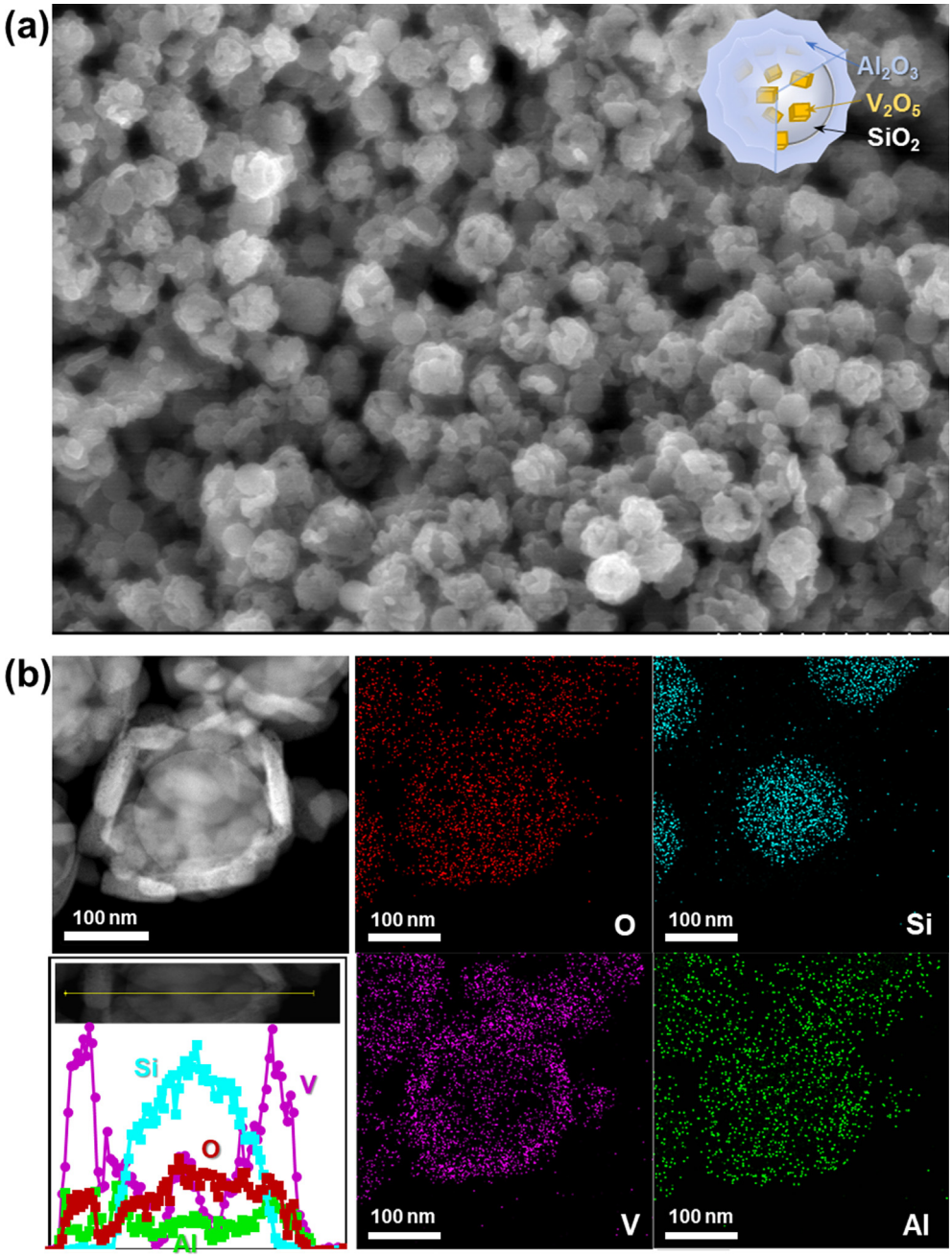

Fig. 2. Structural characterization of $SiO_2@V_2O_5@Al_2O_3$-(50) core@shell nanostructures: (a) SEM image, (b) STEM images with a line-scan EDS spectrum.

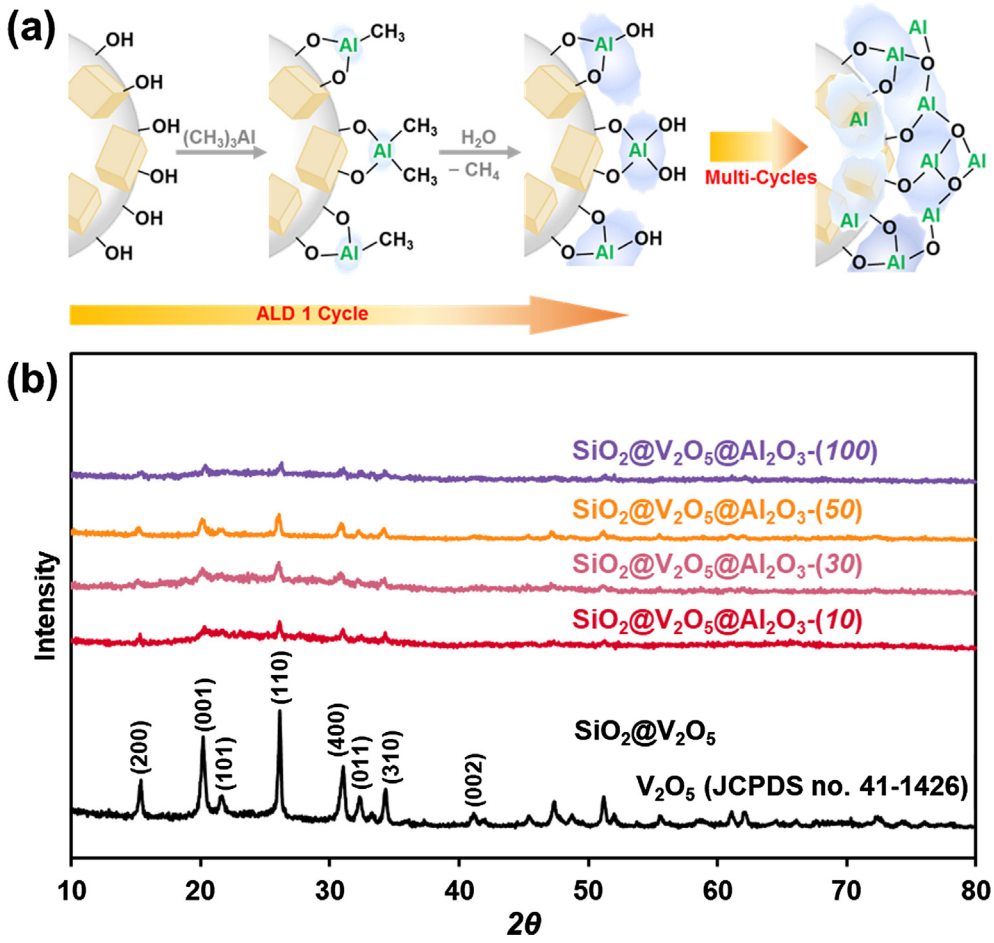

Fig. 3. (a) Schematic illustration of the ALD process used for multicycle coating of Al_2O_3 shells on $SiO_2@V_2O_5$ nanostructures. (b) XRD patterns of $SiO_2@V_2O_5@Al_2O_3$-(10, 30, 50, and 100) nanostructures.

ALD cycles resulted in the deposition of additional alumina layers over $SiO_2@V_2O_5$. The XRD patterns of $SiO_2@V_2O_5$ core@shell catalysts (Fig. 3b) revealed the presence of characteristic peaks of V_2O_5 (*Pmmn*, a = 1.1516, b = 0.3566, c = 0.4372 nm). Application of the Scherrer equation to the (1 1 0) peak allowed the crystallite size of $SiO_2@V_2O_5$ core@shell structures to be estimated as 40.1 nm, which agreed with values obtained by TEM and SEM. However, much weaker XRD peaks were observed for $SiO_2@V_2O_5@Al_2O_3$ core@shell nanostructures (Fig. 3b), since the Al_2O_3 shell was not crystalline. XRD analysis of $SiO_2@V_2O_5@Al_2O_3$-(10, 30, 50, and 100) nanostructures revealed that as the number of ALD cycles increased from 10 to 100, the crystallite size (calculated as mentioned above) increased from 31.3 to 34.6 nm. Two explanations were proposed for this result, namely (a) as-prepared V_2O_5 nanoparticles diffused to Al_2O_3 surfaces with decreased sizes of V_2O_5 and (b) diffraction from the V_2O_5 core was hindered by thick Al_2O_3 shells obtained after an increased number of ALD cycles.

3.2. Thermal stability of V_2O_5 species in core@shell nanostructures

The thermal stability of $SiO_2@V_2O_5$ core@shell catalysts before and after Al_2O_3 deposition was probed by in situ XRD analysis at 100–800 °C under 4% CH_4, 4% O_2, and balance Ar. Fig. 4a shows that the characteristic XRD peaks of V_2O_5 were preserved in $SiO_2@V_2O_5$ core@shells, while the peak intensity increased with increasing temperature up to 750 °C. The crystallite size calculated by the Scherrer equation for V_2O_5 nanoparticles increased from 50.8 nm at 100 °C to 77.9 nm at 750 °C. At a high temperature, the outer V_2O_5 nanoparticles gradually collapsed. Above 800 °C, structural dissociation decreased XRD peak resolution, and only the main peaks were observed. Conversely, $SiO_2@V_2O_5@Al_2O_3$-(50) core@shell nanostructures maintained their XRD peak intensities up to 800 °C, which demonstrated that the presence of Al_2O_3 shells prevented the aggregation of core V_2O_5 nanoparticles at a high temperature (Fig. 4b). Detailed information on the particle size of core V_2O_5 in $SiO_2@V_2O_5@Al_2O_3$ core@shell nanostructures determined by in situ XRD analysis is provided in Table S2.

Interestingly, new peaks are recognized in $SiO_2@V_2O_5@Al_2O_3$ core@shell nanostructures beyond 700 °C (Fig. 4b). When we examined the possibility of any other crystalline structure of either alumina or vanadium oxide, these were matched neither to crystalline aluminas such as alpha, gamma, and theta, nor to vanadium oxides including V_2O_3, V_4O_7, and VO_2. The high-resolution TEM images in Fig. S1 show that the thin Al_2O_3 shell did not show any crystallinity. Previous studies reported that the $AlVO_4$ phase formed from a solid-state reaction between V_2O_5 and Al_2O_3 beyond 570 °C [42–44] and the additional XRD peaks in the range 26–30° (Fig. 4b) corresponded to the characteristic peaks of $AlVO_4$. Based on these results, as the temperature increased, thin alumina shells were not crystallized but generated new $AlVO_4$ species resulting from a solid-state reaction between V_2O_5 and Al_2O_3 above 700 °C.

3.3. Catalytic oxidation of methane to formaldehyde

Methane oxidation over $SiO_2@V_2O_5@Al_2O_3$ core@shell nanostructures with controlled Al_2O_3 shell thickness was carried out in

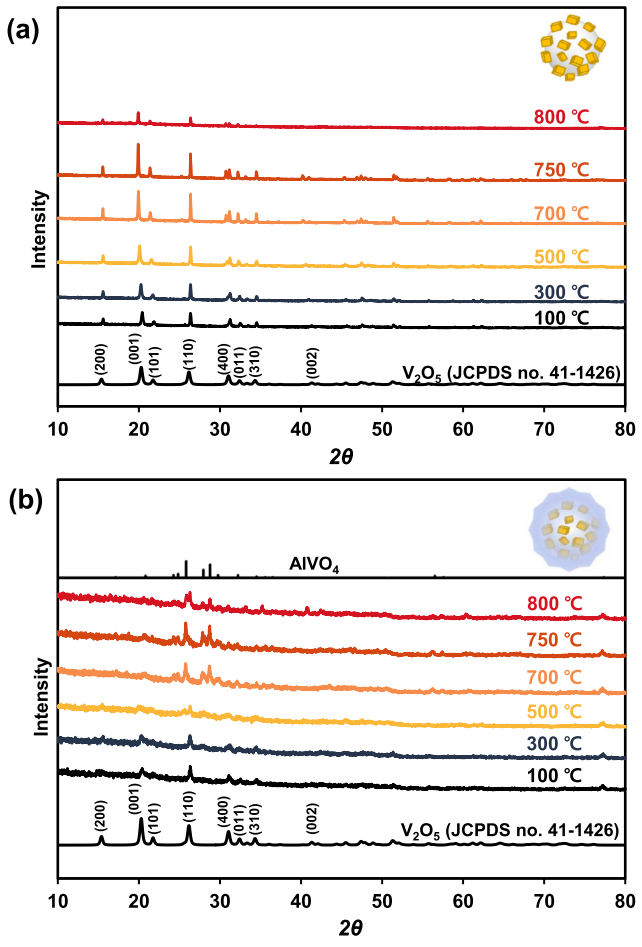

Fig. 4. In situ XRD patterns of (a) SiO_2@V_2O_5 and (b) SiO_2@V_2O_5@Al_2O_3-(50) nanostructures.

a laboratory-scale flow reactor operated at 600 °C at a CH_4/O_2 ratio of 1:1 (v/v). Fig. 5a shows methane conversion as a function of time on stream over SiO_2@V_2O_5@Al_2O_3-(*50*) nanostructures at 600 °C.

The initially observed gradual increase of conversion with time on stream was followed by an abrupt change at 6 h (at which point the product selectivity changed as well) and subsequent saturation to the maximum. Abrupt changes were also found in other SiO_2@V_2O_5@Al_2O_3 nanostructures with a different thickness of the Al_2O_3 shell (Fig. S2). This behavior was ascribed to a structural rearrangement of the catalyst, but more detailed information is required for a sound conclusion. Methane conversion of the SiO_2@V_2O_5@Al_2O_3-(*50*) nanostructures reached ~22.2%, and the corresponding HCHO, CO, and CO_2 selectivities equaled 57.8, 27.4, and 14.8%, respectively (Table 1). Beyond 35 h, the overall conversion and selectivity stayed constant, demonstrating that the SiO_2@V_2O_5@Al_2O_3-(50) nanostructures were thermally stable by having long-term stability in the high temperature methane oxidation. Additionally, we conducted methane oxidation over SiO_2@V_2O_5@Al_2O_3-(x) nanostructures having different shell thicknesses (Fig. 5b). Notably, whereas the maximum conversion of methane observed for SiO_2@V_2O_5@Al_2O_3-(50) equaled 22.2%, negligible conversion was observed for x = 0–30. Thus, the original SiO_2@V_2O_5 core@shell structures did not show substantial methane oxidation activity because of the instability of V_2O_5 nanoparticles at 600 °C.

TEM imaging of spent catalysts confirmed the agglomeration of vanadium species after the reaction (Fig. S3). When the number of ALD cycles was increased to x = 40, stabilization of core vanadium species resulted in a maximum methane conversion of 12.9%. The protective effect of the Al_2O_3 shell was maximized in SiO_2@V_2O_5@Al_2O_3-(50), which featured strongly enlaced Al_2O_3 shells that still provided enough space for constant exchange of reactants and products, with further shell thickness increases resulting in deteriorated performance; for example, a conversion of only 3.7% was observed for SiO_2@V_2O_5@Al_2O_3-(100) (Table 1 and Fig. S1d). Fig. 5b compares the methane conversions and selectivity yields obtained from various SiO_2@V_2O_5@Al_2O_3-(x) core@shell nanostructures (x = 0, 10, 30, 40, 50, 70, and 100). Nguyen et al. showed that HCHO could be produced with 57.5% selectivity by oxidation of methane (total methane conversion = 6.3%) over V_2O_5/SiO_2 catalysts at a GHSV of 185,000 L kg_{cat}^{-1} h^{-1} and 600 °C.[11] For comparison, we also prepared MCF-17-supported V_2O_5 catalysts with different vanadium loadings. Fig. 5c shows the methane oxidation performance of V_2O_5/*m*-SiO_2 catalysts with vanadium loadings of 1, 3, and 5 wt %, revealing that methane conversion (5.5–5.6%) and HCHO selectivity (65.7–71.2%) obtained at 600 °C were in good agreement with those reported by Nguyen et al. [11]. Table 1 summarizes the methane oxidation performance of core@shell nanostructures with controlled Al_2O_3 shell thicknesses and that of supported V_2O_5/*m*-SiO_2 catalysts, demonstrating that the best methane conversion achieved for SiO_2@V_2O_5@Al_2O_3-(*50*) has never been achieved before for any vanadium-based catalyst at 600 °C [45–50]. Recent research on methane oxidation to formaldehyde shows advanced methane conversion and selectivity toward HCHO over modified vanadium-supported catalysts [45–49]. Loricera et al. reported vanadium oxide-supported silica catalysts prepared by the sol–gel method [45]. They reported 2.3% CH_4 conversion and 33% HCHO selectivity (reaction conditions: 600 °C, GHSV = 2830 mL/min·g_{cat}, CH_4:O_2 = 9). Wallis et al. studied the role of the support pore structure and morphology of VO_x/SBA-15 catalysts [46]. They exhibited 1% CH_4 conversion and 40% HCHO selectivity (reaction conditions: 540–650 °C, GHSV = 360,000 L/kg_{cat}·h, CH_4:O_2 = 9). The same group also discovered that vanadium (2.5 wt%) supported on 0.2 wt% Ti-doped SBA-15 showed higher selectivity to HCHO (46%) with 1.2% CH_4 conversion, compared with VO_x/SBA-15 at 600 °C [47]. Very recently, Dang et al. reported on VO_x/MCM-41 catalysts to study the influence of vanadium sources [48]. They found that vanadyl acetyl acetonate facilitated the highest VO_x density, exhibiting 5% CH_4 conversion and 32% HCHO selectivity (reaction conditions: 600 °C, GHSV = 360,830 L/kg_{cat}·h, CH_4:O_2 = 9). A comparison of the performance of vanadium supported catalysts is summarized in Table S3. Based on the existing results, 2.2% VO_x/SiO_2, developed by Nguyen et al., showed the best CH_4 conversion of 6.3% with 58% HCHO selectivity (reaction conditions: 600 °C, GHSV = 185,000 L/kg_{cat}·h, CH_4:O_2 = 38:13) [11]. When GHSV was 8000 L/kg_{cat}·h, the conversion increased further to 7.7%, while the selectivity toward HCHO decreased to 49%. However, these effects were caused by additional water to the stream. Later, they reported that the water created hydroxylated monomeric species, which influenced the positive effect by enhancing methane oxidation to formaldehyde [49]. Although the reaction conditions, including gas composition, the feed rate (GHSV), and temperature, varied from study to study, SiO_2@V_2O_5@Al_2O_3-(50) nanostructures in our study still exhibit the best catalytic activity, with 22.2% of CH_4 conversion and 57.8% HCHO selectivity at 600 °C under 24,000 mL g_{cat}^{-1} h^{-1}, surpassing all previously known vanadium-based catalysts at 600 °C.

3.4. Characterization of V_2O_5 in SiO_2@V_2O_5@Al_2O_3 core@shell catalysts

The catalytic activity of supported vanadium catalysts is known to depend on the dispersion of vanadium, the nature of vanadium active sites, and the metal–support interaction determined by the selection of suitable oxide supports [51–56]. For many forms of

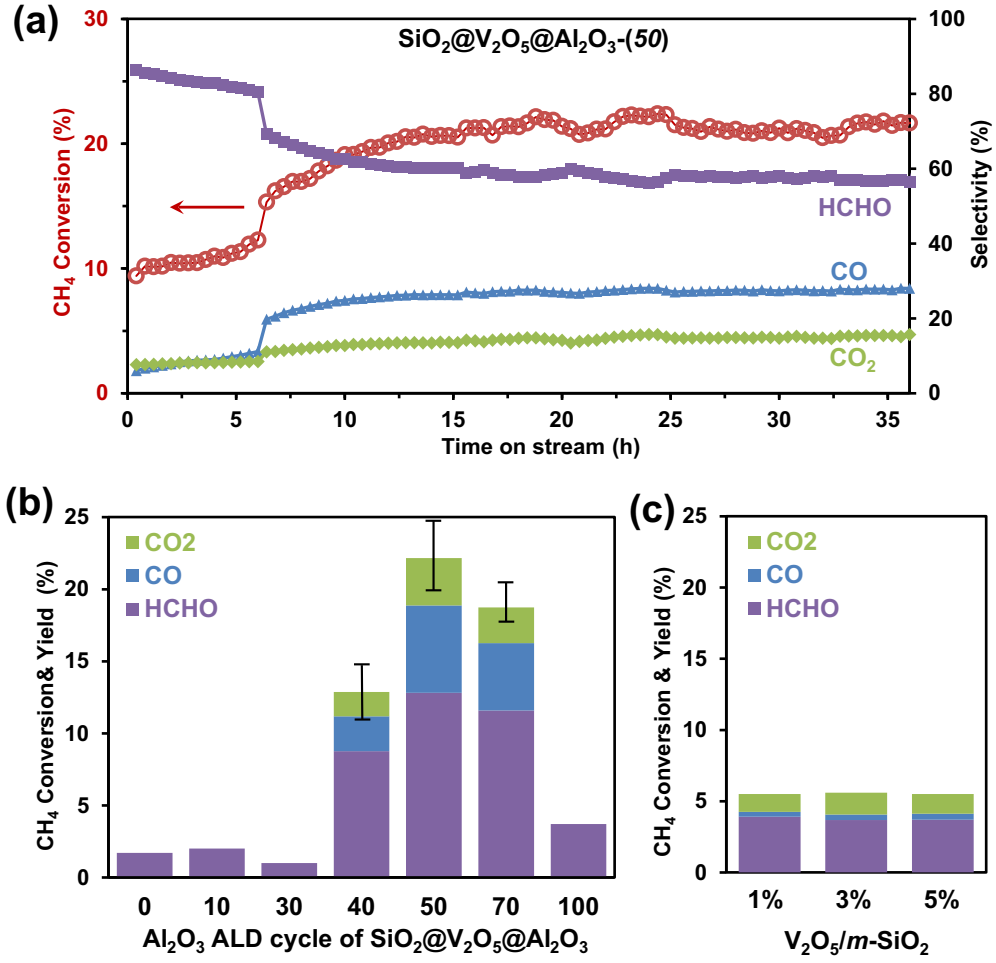

Fig. 5. Methane oxidation performance of various $SiO_2@V_2O_5@Al_2O_3$ core@shell nanostructures and supported V_2O_5/m-SiO_2 catalysts at 600 °C. (a) Methane conversion and selectivity obtained for $SiO_2@V_2O_5@Al_2O_3$-(50) nanostructures as a function of time on stream. (b) Comparison of $SiO_2@V_2O_5@Al_2O_3$-(*x*) core@shell nanostructures in terms of achieved methane conversion and product yield. (c) Methane oxidation performance of V_2O_5/m-SiO_2 catalysts with vanadium loadings of 1, 3, and 5 wt%. Reaction conditions: 40 sccm of 1:1 (v/v) CH_4/O_2, 600 °C, atmospheric pressure, 0.1 g catalyst.

Table 1
Methane oxidation performance of selected vanadium-based catalysts obtained at a CH_4/O_2 ratio of 1:1 (v/v) and a reaction temperature of 600 °C (n.d. = not detected).[a]

Catalyst	ALD cycle no.	Conversion (%)	TOF (s^{-1})	Selectivity (%)		
				HCHO	CO	CO_2
$SiO_2@V_2O_5$	0	1.7	0.02	n.d.	0	0
$SiO_2@V_2O_5@Al_2O_3$-(10)	10	2.0	0.02	n.d.	0	0
$SiO_2@V_2O_5@Al_2O_3$-(30)	30	1.0	0.01	n.d.	0	0
$SiO_2@V_2O_5@Al_2O_3$-(40)	40	12.9	0.10	68	19	13
$SiO_2@V_2O_5@Al_2O_3$-(50)	50	22.2	0.14	58	27	15
$SiO_2@V_2O_5@Al_2O_3$-(70)	70	18.7	0.13	62	25	13
$SiO_2@V_2O_5@Al_2O_3$-(*1 0 0*)	100	3.7	0.04	100	0	0
V_2O_5/m-SiO_2 1 wt%		5.5	0.03	71	6	23
V_2O_5/m-SiO_2 3 wt%		5.6	0.01	66	7	27
V_2O_5/m-SiO_2 5 wt%		5.5	>0.01	67	8	25

[a] Each reaction was conducted more than three times for reproducibility. The conversion and TOF are mean values and the deviation is within 15%.

catalytic oxidation, including the partial oxidation of hydrocarbons, oxidative dehydrogenation of alkanes to alkenes, selective catalytic reduction of NO_x, and the oxidation of SO_2 [52,57–59], isolated tetrahedral (T_d) vanadium oxide species containing terminal V=O groups have been proposed as active sites [56,60–62]. To characterize vanadium species in $SiO_2@V_2O_5@Al_2O_3$ core@shell nanostructures and compare them with those in V_2O_5/m-SiO_2 catalysts, the above materials were analyzed by Raman spectroscopy, H_2 TPR, and diffuse reflectance UV–vis spectroscopy.

Raman spectroscopy is a powerful tool for characterizing the dispersion of vanadium oxide species over high-surface-area supports [60,63–65]. Fig. 6a shows Raman spectra of $SiO_2@V_2O_5$ and $SiO_2@V_2O_5@Al_2O_3$-(*50*) core@shell nanostructures at 600 °C, revealing the presence of bands at 995 (V=O), 703, 406, 305, and 285 cm^{-1} in all cases and thus indicating that all catalysts contained crystalline V_2O_5 [53,66,67]. Although the Raman spectra of 3 wt% V_2O_5/m-SiO_2 were similar to those of core@shell catalysts prepared from crystalline V_2O_5, a shoulder peak at 1040 cm^{-1}

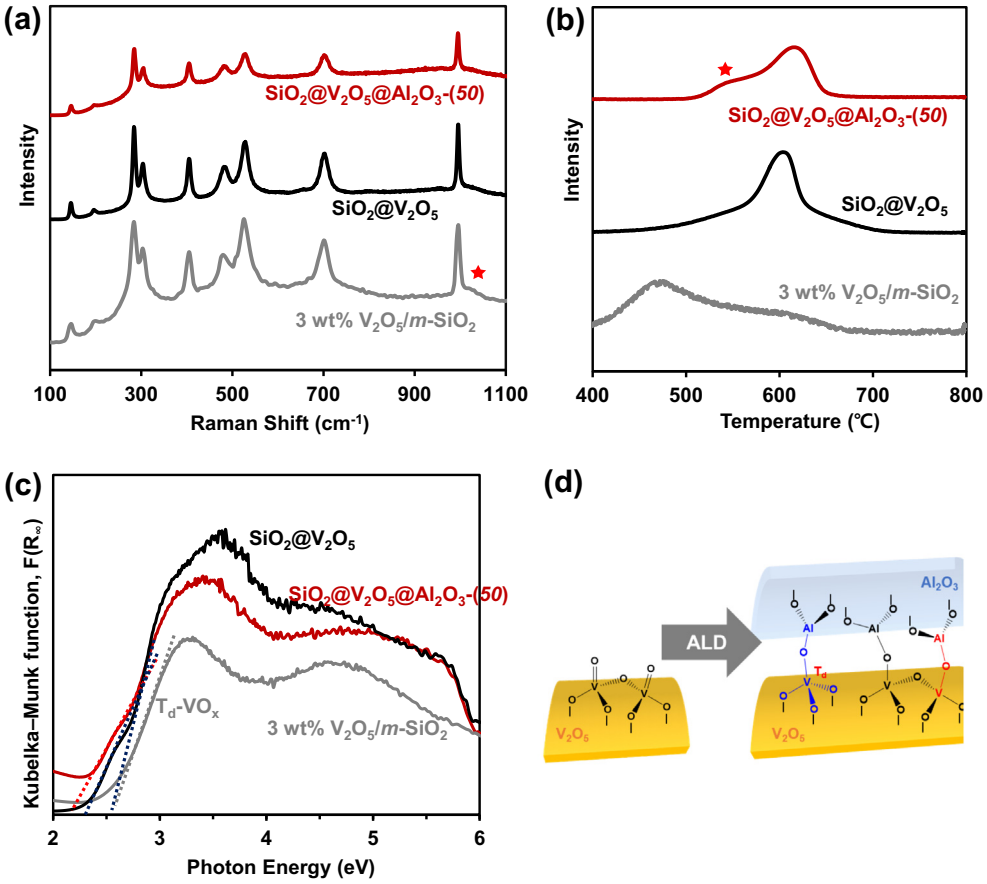

Fig. 6. (a) Raman spectra, (b) H_2 TPR curves, and (c) UV–vis diffuse reflectance spectra of $SiO_2@V_2O_5$ and $SiO_2@V_2O_5@Al_2O_3$-(*50*) core@shell nanostructures, and 3 wt% V_2O_5/*m*-SiO_2. (d) Formation of new T_d vanadium species and V—O—Al bonds by a reaction between V_2O_5 and Al_2O_3 in the $SiO_2@V_2O_5@Al_2O_3$ core@shell catalyst.

ascribed to the symmetric V═O stretch of isolated VO_4 species was observed in the former case (Fig. 6a) [51]. Interestingly, as the vanadium content of V_2O_5/*m*-SiO_2 decreased to 1 wt%, the above shoulder peak became dominant (Fig. S4), which indicated that the relative content of crystalline V_2O_5 in V_2O_5/*m*-SiO_2 catalysts decreased at low vanadium loadings. For all V_2O_5/*m*-SiO_2 catalysts, TEM imaging could not discriminate between well-dispersed small vanadium species and *m*-SiO_2 (Fig. S5). After methane oxidation at 600 °C, the major Raman spectra of $SiO_2@V_2O_5@Al_2O_3$-(*50*) core@shell nanostructures were still observed, demonstrating high thermal stabililty (Fig. S6a).

The dispersion and type of active vanadium species were evaluated by H_2 TPR. In previous reports, the low-temperature H_2 TPR reduction peak observed at 460–500 °C was ascribed to the reduction of V^{5+} in highly dispersed monomeric species to V^{3+} [51,68–70]. As the vanadium loading increased, the reduction peaks shifted to higher temperatures as a consequence of reduction kinetics (i.e., because of the effect of the partial pressure of water formed during reduction and the effect of the actual reactant concentration described by the Kissinger equation) [68–72]. The high-temperature reduction peak at ~600 °C was assigned to the reduction of vanadium in polymeric and bulklike V_2O_5 species [50,73]. The TPR profiles in Fig. 6b show that 3 wt% V_2O_5/*m*-SiO_2 contained highly disperse monomeric species as well as a small amount of V_2O_5 species, in good agreement with the results of Raman spectroscopy analysis. Pristine $SiO_2@V_2O_5$ contained only bulk V_2O_5 species, which was ascribed to the size of V_2O_5 nanoparticles (35 nm). Conversely, the $SiO_2@V_2O_5@Al_2O_3$-(50) core@shell catalyst contained both V_2O_5 and highly disperse monomeric species, exhibiting two broad TPR bands at 550 and 620 °C. In the case of spent $SiO_2@V_2O_5@Al_2O_3$-(*50*) after methane oxidation, a dominant high-temperature band at 600 °C was observed, together with a low-temperature band of negligible intensity (Fig. S6b).

Finally, diffuse reflectance UV–vis spectroscopy was applied to investigate the dispersion and local structure of supported vanadium catalysts [74–76]. For dispersed V_2O_5 domains, Barton et al. plotted the square root of the Kubelka–Munk function multiplied by the photon energy [67] versus the photon energy to estimate the position of the absorption edge by extrapolating the linear part of the rising curve to zero, showing that the obtained values could be used to determine the average domain size of oxide nanoparticles [75,77]. The diffuse reflectance UV–vis spectra of investigated catalysts are shown in Fig. 6c. The absorption band just above 3 eV was ascribed to VO_x species with T_d coordination [66], while that around 5.5 eV evidenced the presence of monomeric T_d species [68,78,79]. The absorption edge positions of 3 wt% V_2O_5/*m*-SiO_2 (2.6 eV) and $SiO_2@V_2O_5$/$SiO_2@V_2O_5@Al_2O_3$-(*50*) (<2.4 eV) indicated that the former catalyst contained homogeneous T_d VO_x species with a smaller domain size than that of the other two catalysts. The low-energy shoulder observed for core@shell catalysts comprising 35 -nm V_2O_5 nanoparticles was ascribed to the bimodal size distribution of crystalline V_2O_5 species, which was not observed for V_2O_5/*m*-SiO_2. Notably, no shoulder was observed for other V_2O_5/*m*-SiO_2 catalysts (1 and 5 wt% loading; Fig. S7). Furthermore, the size distributions deduced from shoulder peaks were different for $SiO_2@V_2O_5$ and $SiO_2@V_2O_5@Al_2O_3$-(50) core@shell catalysts, demonstrating that the properties of crystalline V_2O_5 species are changed by the deposition of Al_2O_3 shells.

Since the interaction between V_2O_5 and Al_2O_3 influenced the catalytic performance, we carried out methane oxidation over conventional V_2O_5/Al_2O_3 catalysts. When V_2O_5/Al_2O_3 catalysts were prepared by impregnation with different vanadium loadings of 3 and 5 wt% and the reaction was tested, negligible conversion was obtained (less than 2% methane conversion) for both catalysts. These results were agreement with the previous study conducted by Koranne et al. [50]. They compared the activity and selectivity of silica- and- alumina-supported vanadium oxide catalysts and found that V_2O_5/Al_2O_3 catalysts showed very low methane conversion, producing no formaldehyde, in contrast to V_2O_5/SiO_2. It was revealed that V_2O_5/Al_2O_3 catalysts were not suitable for methane oxidation to formaldehyde. When we characterized 3 and 5 wt% V_2O_5/Al_2O_3 catalysts prepared by impregnation, we could not find any distinct features in H_2 TPR and UV–vis diffuse reflectance spectra of the two catalysts (Fig. S8). Martinez-Huerta et al. reported that neither terminal V=O nor bridging V—O—V bonds influenced the chemical properties of the supported VO_x/Al_2O_3 catalysts; instead the bridging V—O—Al bond was the catalytic active site for oxidative dehydrogenation of ethane to ethylene [42].

The combined results indicate that V_2O_5 nanoparticles formed on SiO_2 spheres were identified as crystalline V_2O_5 species, and the additional Al_2O_3 shells of $SiO_2@V_2O_5@Al_2O_3$-(50) were proven to provide new surfaces for creating highly dispersed T_d monomeric species by promoting interactions between Al_2O_3 and V_2O_5 nanoparticles during the ALD process (Fig. 6d). Based on fact that the $AlVO_4$ phase was present in the $SiO_2@V_2O_5@Al_2O_3$ core@shell nanostructures at the elevated temperature, the interaction between Al_2O_3 and V_2O_5 nanoparticles generated bridging V—O—Al bonds in the $AlVO_4$. The highly disperse T_d vanadium species with a V—O—Al bond of the $SiO_2@V_2O_5@Al_2O_3$ core@shell nanostructures were not seen in the conventional V_2O_5/Al_2O_3 catalysts. As a result, the newly formed T_d monomeric vanadium species connected to the V—O—Al bond facilitated methane oxidation at 600 °C and achieve high methane conversion. Additionally, the Al_2O_3 shell protected V_2O_5 nanoparticles against sintering.

4. Conclusions

Here, we successfully prepared $SiO_2@V_2O_5@Al_2O_3$ core@shell nanostructures by hydrothermal synthesis and subsequent ALD. Methane conversion was carried out over $SiO_2@V_2O_5@Al_2O_3$ core@shell nanostructures and V_2O_5/m-SiO_2 catalysts in a flow reactor at a CH_4/O_2 ratio of 1:1 (v/v) and 600 °C, and the major reaction products were identified as HCHO, CO, CO_2, and H_2. $SiO_2@V_2O_5@Al_2O_3$-(50) exhibited methane conversion of 22.2% and formaldehyde selectivity of 57.8%, whereas 1, 3, and 5 wt% V_2O_5/m-SiO_2 catalysts prepared by impregnation exhibited methane conversions of 5.5–5.6% and HCHO selectivities of 65.7–71.2% under the same conditions. As the catalytic activity of supported vanadium catalysts largely depends on the dispersion of vanadium and the nature of vanadium active sites, $SiO_2@V_2O_5@Al_2O_3$ core@shell catalysts were characterized by Raman spectroscopy, H_2 TPR, and diffuse reflectance UV–vis spectroscopy, which revealed that the highly disperse T_d monomeric species with V—O—Al bonds found in $SiO_2@V_2O_5@Al_2O_3$-(50) were not present in $SiO_2@V_2O_5$. Thus, these new T_d monomeric vanadium species and V—O—Al bonds were produced by the interactions between Al_2O_3 and V_2O_5 nanoparticles during the ALD process in the presence of crystalline V_2O_5 species, accounting for the high conversion of methane during oxidation at 600 °C. The developed strategy for the preparation of highly active and stable core@shell nanocatalysts is expected not only to provide robust oxide shells protecting against sintering during high-temperature reactions, but also to anchor the new active species inside shells and thus realize outstanding catalytic performance.

Acknowledgment

This research was supported by C1 Gas Refinery Program through the National Research Foundation of Korea (NRF) funded by the Ministry of Science, ICT & Future Planning (2015M3D3A1A01064899), South Korea.

Appendix A. Nomenclature

ALD	atomic layer deposition
BET	Brunauer–Emmett–Teller
EDS	energy-dispersive X-ray spectroscopy
GHSV	gas hourly space velocity
SEM	scanning electron microscopy
TEM	transmission electron microscopy
TEOS	tetraethyl orthosilicate
TMA	trimethylaluminum
TPR	temperature-programmed reduction
XRD	X-ray diffraction

Appendix B. Supplementary material

Supplementary data to this article can be found online at https://doi.org/10.1016/j.jcat.2018.09.027.

References

[1] P. Tang, Q. Zhu, Z. Wu, D. Ma, Methane activation: the past and future, Energy Environ. Sci. 7 (2014) 2580–2591.
[2] E. McFarland, Unconventional chemistry for unconventional natural gas, Science 338 (2012) 340–342.
[3] A.T. Ashcroft, A.K. Cheetham, J.S. Foord, M.L.H. Green, C.P. Grey, A.J. Murrell, P. D.F. Vernon, Selective oxidation of methane to synthesis gas-using transition-metal catalysts, Nature 344 (1990) 319–321.
[4] T.V. Choudhary, V.R. Choudhary, Energy-efficient syngas production through, catalytic oxy-methane reforming reactions, Angew. Chem. Int. Ed. 47 (2008) 1828–1847.
[5] M. Ravi, M. Ranocchiari, J.A. van Bokhoven, A Critical assessment of the direct catalytic oxidation of methane to methanol, Angew. Chem. Int. Ed. 56 (2017) 16464–16483.
[6] G.J. Hutchings, M.S. Scurrell, J.R. Woodhouse, Oxidative coupling of methane using oxide catalysts, Chem. Soc. Rev. 18 (1989) 251–283.
[7] J.H. Lunsford, The catalytic oxidative coupling of methane, Angew. Chem. Int. Ed. Engl. 34 (1995) 970–980.
[8] J.H. Lunsford, Catalytic conversion of methane to more useful chemicals and fuels: a challenge for the 21st century, Catal. Today 63 (2000) 165–174.
[9] B.C. Enger, R. Lodeng, A. Holmen, A review of catalytic partial oxidation of methane to synthesis gas with emphasis on reaction mechanisms over transition metal catalysts, Appl. Catal. A 346 (2008) 1–27.
[10] A. Parmaliana, F. Arena, Working mechanism of oxide catalysts in the partial oxidation of methane to formaldehyde. I. Catalytic behaviour of SiO_2, MoO_3/SiO_2, V_2O_5/SiO_2, TiO_2, and V_2O_5/TiO_2 systems, J. Catal. 167 (1997) 57–65.
[11] L.D. Nguyen, S. Loridant, H. Launay, A. Pigamo, J.L. Dubois, J.M.M. Millet, Study of new catalysts based on vanadium oxide supported on mesoporous silica for the partial oxidation of methane to formaldehyde: catalytic properties and reaction mechanism, J. Catal. 237 (2006) 38–48.
[12] F. Arena, A. Parmaliana, Scientific basis for process and catalyst design in the selective oxidation of methane to formaldehyde, Acc. Chem. Res. 36 (2003) 867–875.
[13] R. Pitchai, K. Klier, Partial oxidation of methane, Catal. Rev. Sci. Eng. 28 (1986) 13–88.
[14] Y.H. Chin, C. Buda, M. Neurock, E. Iglesia, Consequences of metal-oxide interconversion for C-H bond activation during CH_4 reactions on Pd catalysts, J. Am. Chem. Soc. 135 (2013) 15425–15442.
[15] J.J. Willis, E.D. Goodman, L.H. Wu, A.R. Riscoe, P. Martins, C.J. Tassone, M. Cargnello, Systematic identification of promoters for methane oxidation catalysts using size- and composition-controlled Pd-based bimetallic nanocrystals, J. Am. Chem. Soc. 139 (2017) 11989–11997.
[16] Y. Kwon, T.Y. Kim, G. Kwon, J. Yi, H. Lee, Selective activation of methane on single-atom catalyst of rhodium dispersed on zirconia for direct conversion, J. Am. Chem. Soc. 139 (2017) 17694–17699.

[17] S. Kasztelan, J.B. Moffat, Partial oxidation of methane by oxygen over silica, J. Chem. Soc. Chem. Commun. 1663–1664 (1987).
[18] G.N. Kastanas, G.A. Tsigdinos, J. Schwank, Selective oxidation of methane over vycor glass, quartz glass and various silica, magnesia and alumina surfaces, Appl. Catal. 44 (1988) 33–51.
[19] Q. Sun, J.I. Dicosimo, R.G. Herman, K. Klier, M.M. Bhasin, Selective oxidation of methane to formaldehyde and C_2 hydrocarbons over double layered Sr/La_2O_3 and MoO_3/SiO_2 catalyst bed, Catal. Lett. 15 (1992) 371–376.
[20] A. Parmaliana, F. Frusteri, A. Mezzapica, D. Miceli, M.S. Scurrell, N. Giordano, A basic approach to evaluate methane partial oxidation catalysts, J. Catal. 143 (1993) 262–274.
[21] A. Guerrero-Martínez, J. Pérez-Juste, L.M. Liz-Marzán, Recent progress on silica coating of nanoparticles and related nanomaterials, Adv. Mater. 22 (2010) 1182–1195.
[22] S.H. Joo, J.Y. Park, C.K. Tsung, Y. Yamada, P.D. Yang, G.A. Somorjai, Thermally stable Pt/mesoporous silica core-shell nanocatalysts for high-temperature reactions, Nat. Mater. 8 (2009) 126–131.
[23] Y. Dai, B. Lim, Y. Yang, C.M. Cobley, W. Li, E.C. Cho, B. Grayson, P.T. Fanson, C.T. Campbell, Y. Sun, A sinter-resistant catalytic system based on platinum nanoparticles supported on TiO_2 nanofibers and covered by porous silica, Angew. Chem. 122 (2010) 8341–8344.
[24] M. Feyen, C. Weidenthaler, R. Güttel, K. Schlichte, U. Holle, A.H. Lu, F. Schüth, High-temperature stable, iron-based core–shell catalysts for ammonia decomposition, Chem. Eur. J. 17 (2011) 598–605.
[25] J. Ge, Q. Zhang, T. Zhang, Y. Yin, Core–satellite nanocomposite catalysts protected by a porous silica shell: controllable reactivity, high stability, and magnetic recyclability, Angew. Chem. 120 (2008) 9056–9060.
[26] Q. Zhang, I. Lee, J.B. Joo, F. Zaera, Y.D. Yin, Core-shell nanostructured catalysts, Acc. Chem. Res. 46 (2013) 1816–1824.
[27] I. Lee, J.B. Joo, Y. Yin, F. Zaera, A yolk@ shell nanoarchitecture for Au/TiO_2 catalysts, Angew. Chem. 123 (2011) 10390–10393.
[28] P.M. Arnal, M. Comotti, F. Schüth, High-temperature-stable catalysts by hollow sphere encapsulation, Angew. Chem. 118 (2006) 8404–8407.
[29] M. Cargnello, J.D. Jaén, J.H. Garrido, K. Bakhmutsky, T. Montini, J.C. Gámez, R. Gorte, P. Fornasiero, Exceptional activity for methane combustion over modular $Pd@CeO_2$ subunits on functionalized Al_2O_3, Science 337 (2012) 713–717.
[30] X. Huang, C. Guo, J. Zuo, N. Zheng, G.D. Stucky, An assembly route to inorganic catalytic nanoreactors containing sub-10-nm gold nanoparticles with anti-aggregation properties, Small 5 (2009) 361–365.
[31] S. Ikeda, S. Ishino, T. Harada, N. Okamoto, T. Sakata, H. Mori, S. Kuwabata, T. Torimoto, M. Matsumura, Ligand-free platinum nanoparticles encapsulated in a hollow porous carbon shell as a highly active heterogeneous hydrogenation catalyst, Angew. Chem. 118 (2006) 7221–7224.
[32] J. Lu, B. Fu, M.C. Kung, G. Xiao, J.W. Elam, H.H. Kung, P.C. Stair, Coking-and sintering-resistant palladium catalysts achieved through atomic layer deposition, Science 335 (2012) 1205–1208.
[33] B.J. O'Neill, D.H.K. Jackson, J. Lee, C. Canlas, P.C. Stair, C.L. Marshall, J.W. Elam, T. F. Kuech, J.A. Dumesic, G.W. Huber, Catalyst design with atomic layer deposition, ACS Catal. 5 (2015) 1804–1825.
[34] S.T. Christensen, H. Feng, J.L. Libera, N. Guo, J.T. Miller, P.C. Stair, J.W. Elam, Supported Ru-Pt bimetallic nanoparticle catalysts prepared by atomic layer deposition, Nano Lett. 10 (2010) 3047–3051.
[35] T.M. Onn, S.Y. Zhang, L. Arroyo-Ramirez, Y.C. Chung, G.W. Graham, X.Q. Pan, R. J. Gorte, Improved thermal stability and methane-oxidation activity of Pd/Al_2O_3 catalysts by atomic layer deposition of ZrO_2, ACS Catal. 5 (2015) 5696–5701.
[36] Y.S. Jung, A.S. Cavanagh, A.C. Dillon, M.D. Groner, S.M. George, S.H. Lee, Enhanced stability of $LiCoO_2$ cathodes in lithium-ion batteries using surface modification by atomic layer deposition, J. Electrochem. Soc. 157 (2010) A75–A81.
[37] W. Stober, A. Fink, E. Bohn, Controlled growth of monodisperse silica spheres in micron size range, J. Colloid Interface Sci. 26 (1968) 62–69.
[38] J. Liu, Y.C. Zhou, J.B. Wang, Y. Pan, D.F. Xue, Template-free solvothermal synthesis of yolk-shell V_2O_5 microspheres as cathode materials for Li-ion batteries, Chem. Commun. 47 (2011) 10380–10382.
[39] Y. Han, S.S. Lee, J.Y. Ying, Spherical siliceous mesocellular foam particles for high-speed size exclusion chromatography, Chem. Mater. 19 (2007) 2292–2298.
[40] T. Sugino, A. Kido, N. Azuma, A. Ueno, Y. Udagawa, Partial oxidation of methane on silica-supported silicomolybdic acid catalysts in an excess amount of water vapor, J. Catal. 190 (2000) 118–127.
[41] S. Siggia, W. Maxcy, Improved procedure for determination of aldehydes, Anal. Chem. 19 (1947) 1023–1025.
[42] M.V. Martinez-Huerta, X. Gao, H. Tian, I.E. Wachs, J.L.G. Fierro, M.A. Banares, Oxidative dehydrogenation of ethane to ethylene over alumina-supported vanadium oxide catalysts: relationship between molecular structures and chemical reactivity, Catal. Today 118 (2006) 279–287.
[43] J.M. Kanervo, M.E. Harlin, A.O.I. Krause, M.A. Banares, Characterisation of alumina-supported vanadium oxide catalysts by kinetic analysis of H_2-TPR data, Catal. Today 78 (2003) 171–180.
[44] E. Arisi, S.A.P. Sanchez, F. Leccabue, B.E. Watts, G. Bocelli, F. Calderon, G. Calestani, L. Righi, Preparation and characterization of $AlVO_4$ compound, J. Mater. Sci. 39 (2004) 2107–2111.
[45] C.V. Loricera, M.C. Alvarez-Galvan, R. Guil-Lopez, A.A. Ismail, S.A. Al-Sayari, J.L. G. Fierro, Structure and reactivity of sol-gel V/SiO_2 catalysts for the direct conversion of methane to formaldehyde, Top. Catal. 60 (2017) 1129–1139.
[46] P. Wallis, S. Wohlrab, V.N. Kalevaru, M. Frank, A. Martin, Impact of support pore structure and morphology on catalyst performance of VO_x/SBA-15 for selective methane oxidation, Catal. Today 278 (2016) 120–126.
[47] P. Wallis, E. Schonborn, V.N. Kalevaru, A. Martin, S. Wohlrab, Enhanced formaldehyde selectivity in catalytic methane oxidation by vanadia on Ti-doped SBA-15, RSC Adv. 5 (2015) 69509–69513.
[48] T.T.H. Dang, D. Seeburg, J. Radnik, C. Kreyenschulte, H. Atia, T.T.H. Vu, S. Wohlrab, Influence of V-sources on the catalytic performance of VMCM-41 in the selective oxidation of methane to formaldehyde, Catal. Commun. 103 (2018) 56–59.
[49] H. Launay, S. Loridant, A. Pigamo, J.L. Dubois, J.M.M. Millet, Vanadium species in new catalysts for the selective oxidation of methane to formaldehyde: specificity and molecular structure dynamics with water, J. Catal. 246 (2007) 390–398.
[50] M.M. Koranne, J.G. Goodwin, G. Marcelin, Partial oxidation of methane over silica-supported and alumina-supported vanadia catalysts, J. Catal. 148 (1994) 388–391.
[51] G. Du, S. Lim, M. Pinault, C. Wang, F. Fang, L. Pfefferle, G.L. Haller, Synthesis, characterization, and catalytic performance of highly dispersed vanadium grafted SBA-15 catalyst, J. Catal. 253 (2008) 74–90.
[52] A. Khodakov, B. Olthof, A.T. Bell, E. Iglesia, Structure and catalytic properties of supported vanadium oxides: Support effects on oxidative dehydrogenation reactions, J. Catal. 181 (1999) 205–216.
[53] X.T. Gao, S.R. Bare, B.M. Weckhuysen, I.E. Wachs, In situ spectroscopic investigation of molecular structures of highly dispersed vanadium oxide on silica under various conditions, J. Phys. Chem. B 102 (1998) 10842–10852.
[54] G. Busca, G. Centi, L. Marchetti, F. Trifiro, Chemical and spectroscopic study of the nature of a vanadium-oxide monolayer supported on a high-surface-area TiO_2 anatase, Langmuir 2 (1986) 568–577.
[55] K. Inumaru, M. Misono, T. Okuhara, Structure and catalysis of vanadium oxide overlayers on oxide supports, Appl. Catal. A 149 (1997) 133–149.
[56] N. Das, H. Eckert, H.C. Hu, I.E. Wachs, J.F. Walzer, F.J. Feher, Bonding states of surface vanadium(V) oxide phases on silica: Structural characterization by ^{51}V NMR and raman spectroscopy, J. Phys. Chem. 97 (1993) 8240–8243.
[57] U.S. Ozkan, T.A. Harris, B.T. Schilf, The partial oxidation of C_5 hydrocarbons over vanadia-based catalysts, Catal. Today 33 (1997) 57–71.
[58] G.C. Bond, S.F. Tahir, Vanadium-oxide monolayer catalysts - preparation, characterization and catalytic activity, Appl. Catal. 71 (1991) 1–31.
[59] G.A. Du, S.Y. Lim, Y.H. Yang, C. Wang, L. Pfefferle, G.L. Haller, Catalytic performance of vanadium incorporated MCM-41 catalysts for the partial oxidation of methane to formaldehyde, Appl. Catal. A 302 (2006) 48–61.
[60] I.E. Wachs, B.M. Weckhuysen, Structure and reactivity of surface vanadium oxide species on oxide supports, Appl. Catal. A 157 (1997) 67–90.
[61] S. Irusta, L.M. Cornaglia, E.E. Miro, E.A. Lombardo, The role of V=O sites on the oxidation of methane to formaldehyde over V/SiO_2, J. Catal. 156 (1995) 167–170.
[62] M. Iwamoto, J. Hirata, K. Matsukami, S. Kagawa, Catalytic-oxidation by oxide radical ions. 1. One-step hydroxylation of benzene to phenol over group 5 and 6 oxides supported on silica gel, J. Phys. Chem. 87 (1983) 903–905.
[63] J.H. Kwak, J.E. Herrera, J.Z. Hu, Y. Wang, C.H.F. Peden, A new class of highly dispersed VO_x catalysts on mesoporous silica: synthesis, characterization, and catalytic activity in the partial oxidation of ethanol, Appl. Catal. A 300 (2006) 109–119.
[64] F. Roozeboom, M.C. Mittelmeijerhazeleger, J.A. Moulijn, J. Medema, V.H.J. Debeer, P.J. Gellings, Vanadium-oxide monolayer catalysts. 3. A raman-spectroscopic and temperature-programmed reduction study of monolayer and crystal-type vanadia on various supports, J. Phys. Chem. 84 (1980) 2783–2791.
[65] I.E. Wachs, Raman and IR studies of surface metal oxide species on oxide supports: Supported metal oxide catalysts, Catal. Today 27 (1996) 437–455.
[66] D.E. Keller, T. Visser, F. Soulimani, D.C. Koningsberger, B.M. Weckhuysen, Hydration effects on the molecular structure of silica-supported vanadium oxide catalysts: a combined IR, Raman, UV-vis and EXAFS study, Vibrat. Spectrosc. 43 (2007) 140–151.
[67] X.T. Gao, M.A. Banares, I.E. Wachs, Ethane and n-butane oxidation over supported vanadium oxide catalysts: an in situ UV-visible diffuse reflectance spectroscopic investigation, J. Catal. 188 (1999) 325–331.
[68] R. Bulanek, P. Cicmanec, H. Sheng-Yang, P. Knotek, L. Capek, M. Setnicka, Effect of preparation method on nature and distribution of vanadium species in vanadium-based hexagonal mesoporous silica catalysts: impact on catalytic behavior in propane ODH, Appl. Catal. A 415 (2012) 29–39.
[69] M.D. Soriano, J.A. Cecilia, A. Natoli, J. Jimenez-Jimenez, J.M.L. Nieto, E. Rodriguez-Castellon, Vanadium oxide supported on porous clay heterostructure for the partial oxidation of hydrogen sulphide to sulfur, Catal. Today 254 (2015) 36–42.
[70] H. Berndt, A. Martin, A. Bruckner, E. Schreier, D. Muller, H. Kosslick, G.U. Wolf, B. Lucke, Structure and catalytic properties of VO_x/MCM materials for the partial oxidation of methane to formaldehyde, J. Catal. 191 (2000) 384–400.
[71] H.E. Kissinger, Reaction kinetics in differential thermal analysis, Anal. Chem. 29 (1957) 1702–1706.
[72] H.E. Kissinger, Variation of peak temperature with heating rate in differential thermal analysis, J. Res. Natl. Bur. Stand. 57 (1956) 217–221.

[73] G. Martra, F. Arena, S. Coluccia, F. Frusteri, A. Parmaliana, Factors controlling the selectivity of V_2O_5 supported catalysts in the oxidative dehydrogenation of propane, Catal. Today 63 (2000) 197–207.
[74] J.E. Herrera, J.H. Kwak, J.Z. Hu, Y. Wang, C.H.F. Peden, J. Macht, E. Iglesia, Synthesis, characterization, and catalytic function of novel highly dispersed tungsten oxide catalysts on mesoporous silica, J. Catal. 239 (2006) 200–211.
[75] D.G. Barton, M. Shtein, R.D. Wilson, S.L. Soled, E. Iglesia, Structure and electronic properties of solid acids based on tungsten oxide nanostructures, J. Phys. Chem. B 103 (1999) 630–640.
[76] A. Khodakov, J. Yang, S. Su, E. Iglesia, A.T. Bell, Structure and properties of vanadium oxide zirconia catalysts for propane oxidative dehydrogenation, J. Catal. 177 (1998) 343–351.
[77] R.S. Weber, Effect of local structure on the UV-Visible absorption edges of molybdenum Oxide clusters and supported molybdenum oxides, J. Catal. 151 (1995) 470–474.
[78] R. Bulanek, L. Capek, M. Setnicka, P. Cicmanec, DR UV-vis study of the supported vanadium oxide catalysts, J. Phys. Chem. C 115 (2011) 12430–12438.
[79] G. Catana, R.R. Rao, B.M. Weckhuysen, P. Van Der Voort, E. Vansant, R.A. Schoonheydt, Supported vanadium oxide catalysts: quantitative spectroscopy, preferential adsorption of $V^{4+}/^{5+}$, and Al_2O_3 coating of zeolite Y, J. Phys. Chem. B 102 (1998) 8005–8012.